Title

Substitution Effect on Thiobarbituric Acid End Groups for High Open-Circuit Voltage Non-Fullerene Organic Solar Cells

Journal

ACS Applied Materials & Interfaces, 12(37)

ISSN

1944-8244

Authors

Xiao, Liangang

Kolaczkowski, Matthew A

Min, Yonggang

et al.

Publication Date

2020-09-16

DOI

10.1021/acsami.0c11828

Peer reviewed

Substitution Effect on Thiobarbituric Acid End Groups for High Open Circuit Voltage Non-Fullerene Organic Solar Cell

Liangang Xiao,[a†] Matthew A. Kolaczkowski,[b,c†] Yonggang Min[a] and Yi Liu*[b]

[a]School of Materials and Energy, Guangdong University of Technology, Guangzhou 510006, China

[b]The Molecular Foundry, Lawrence Berkeley National Laboratory, Berkeley, CA, 94720, USA

E-mail: yliu@lbl.gov

[c]Department of Chemistry, University of California, Berkeley, CA, 94720, USA

[†]contributed equally

Abstract: Recent advances in non-fullerene acceptors (NFA) have resulted in significant improvement of power conversion efficiencies (PCEs) of organic solar cells (OSCs). In our efforts to boost open-circuit voltage (V_{OC}) for OSCs, the molecular design employing thiobarbituric acid (TBTA) end groups and a IDTT core gives rise to

NFA with significantly raised lowest unoccupied molecular orbital (LUMO) energy level, which, when paired with PCE10, can achieve V_{OC}s over 1.0 V and decent PCEs that outperform the equivalent devices based on the benchmark ITIC acceptor. While the use of TBTA end group is effective in tuning energy levels, very little is known about how the alkyl substitution on the TBTA group impacts the solar cell performance. To this end, TBTA end groups are alkylated with linear, branched, and aromatic sidechains in an effort to understand the influence on thin film morphology and related device performances. Our study has confirmed the dependence of solar cell performance on the end group substituents. More importantly, we reveal the presence of an ideal window of crystallinity associated with the medium length hydrocarbon chains such as ethyl and benzyl. Deviation to the shorter methyl group makes the acceptor too crystalline to mix with polymer donor and form proper domains, whereas longer and branched alkyl chains are too sterically bulky and hinder charge transport due to nonideal packing. Such findings underline the comprehensive nature of thin film morphology and the subtle end group effects for the design of non-fullerene acceptors.

Keywords: non-fullerene acceptors, sidechains, solar cells,

thiobarbituric acid, window of crystallinity

Introduction

Historically, fullerene based acceptors have dominated the field of organic solar cells (OSCs) for over two decades.[1-8] Solubilized fullerenes with high electron mobilities, such as $PC_{71}BM$ increased solar cell power conversion efficiency (PCE) from below 1% to as high as 11.7%.[9-13] Despite these progresses, fullerene acceptors suffer from a number of inherent limitations. Poor light absorption in the visible region limits the photocurrent generation in fullerene-based solar cells. On the other hand, the low lowest unoccupied molecular orbital (LUMO) energy level pins the open-circuit voltage (V_{OC}) to unsatisfactorily low levels and also limits the scope of compatible donor materials.[14-15]

The disparity has spurred development of new design strategies for the next generation of acceptor materials. This research focus has given rise to entirely new non-fullerene acceptors (NFAs) molecules that overperform fullerene-based materials, with recent advances in NFA-based solar cells reaching performance over 16% PCE.[16-26] The early development of NFAs is based on a benchmark acceptor ITIC,[27] which is a symmetrical molecule containing three functional regions: 1) the electron rich indacenodithieno[3,2-

b]thiophene (IDTT) core, locked into planarity via 2) spirocenters with solubilizing groups, and capped with 3) electron withdrawing 1,1-dicyanomethylene-3-indanone (DCI) end groups. Each of these areas can be functionalized independently, allowing for control over the electronic and physical properties. Due to the inherent acceptor-donor-acceptor structure of ITIC, the highest occupied molecular orbital (HOMO) energy level is predominantly controlled by the electron donating ability of the planar core, while the multifunctional spirocenters not only provide steric bulkiness to prevent self-aggregation, but also increase solubility through the introduction of alkyl groups. On the other hand, the electron-withdrawing strength of the end groups determines the LUMO energy level and minimally impacts the HOMO level. A common strategy to increase efficiency is to lower the acceptor LUMO energy in order to increase the absorption of lower energy light for higher short-circuit current (J_{SC}). Such energy level modification however also results in lower $V_{OC.}$ Alternatively, increasing the acceptor LUMO can greatly improve V_{OC} though often with a tradeoff in J_{SC}.

Based on the modular nature of the ITIC system, new withdrawing groups can be incorporated to raise the LUMO energy level of the acceptor. To this end, thiobarbituric acid (TBTA) end groups have been chosen due to their weakly electron-withdrawing

character. The TBTA group has been utilized in a fluorene based acceptor for organic solar cells to provide an exceptional V_{OC} of 1.15 V.[31] However, the J_{SC} in this system is limited to 7.5 mA cm^{-2}, leaving significant room for improvement. We have recently demonstrated a TBTA end-capped IDTT acceptor capable of achieving 9.2% PCE in binary solar cells using PCE10 as the donor, which resulted in a V_{OC} of 1.02 V, significantly higher than that of ITIC (0.825 V) without compromises in $J_{SC.}$[32] Huang group has reported similar results based on the same acceptor design.[33] In addition, we have incorporated an indacenodithiophene (IDT) based acceptor in a ternary system with a PCE up to 12.3%.[34]

The end groups are postulated to be a location of significant π overlap between molecules which is necessary for electronic communication in the active layer and efficient charge transport.[35] This makes intermolecular and steric interactions between end groups of critical importance. Despite this, prior to this work, only ethyl chains have been explored as the *N*-substituents on TBTA. The lack of understanding about end group composition warrants an in-depth study of their effect on morphology and the device performance. Alkyl chains can easily be appended to the TBTA core to affect intermolecular interactions and moderate charge separation and transport in active layers. In this contribution, a

series of TBTAs with various alkyl chain lengths and types have been prepared, incorporated into IDTT based non-fullerene acceptors, and examined as active materials to understand their impact on organic solar cells.

Results and Discussion

A range of alkyl chain length and shapes have been chosen as the *N*-substituents on the TBTA end group. Methyl, ethyl, and *n*-octyl chains are used in order to compare linear chain length effects on solubility and end group interactions. The 2-ethylhexyl chain is an isomer of the *n*-octyl chain, allowing for a direct comparison between linear and branched effects on steric interactions. A benzyl substituent is also chosen as a means to impose intermolecular interactions via additional π-surface area.

None of the TBTA derivatives except the *N*-ethyl substituted **1b** are commercially available and are synthesized following a modified protocol.[36] As shown in **Scheme 1a**, the reaction of alkylamines with carbon disulfide proceed smoothly under mild conditions to give the alkylcarbamodithioic acids, which subsequently eliminate H_2S to form the isothiocyanates at elevated temperatures. The isothiocyanates undergo a second addition with the primary amine to form the respective dialkylthioureas **1**, which react with diethyl

malonate in refluxing EtOH in the presence of NaOEt to afford TBTA derivatives **2**. The yield of the cyclization reaction decreases as the chain length is increased or branching is introduced. The condensation of ITIC-dialdehyde with TBTA **2a-e** is rapid and efficient (**Scheme 1b**), converting the bright yellow aldehyde to deep blue acceptors with strong absorption in the red portion of the spectrum.

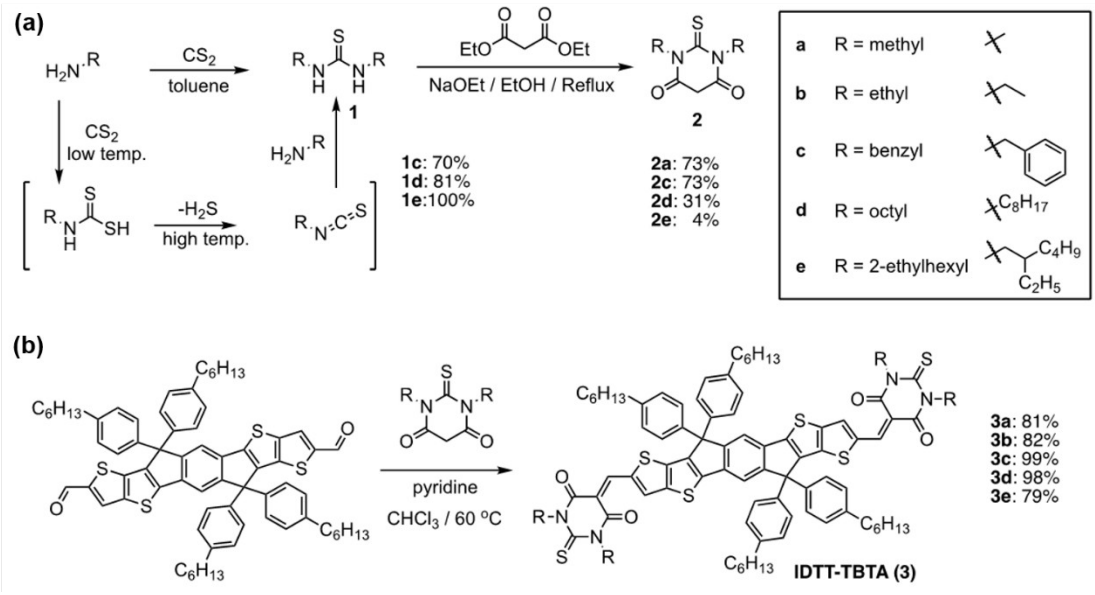

Scheme 1. Synthesis of alkyl-substituted TBTA derivatives **2** and the subsequent reaction to give the IDTT-TBTA acceptors **3a**-**e**.

In order to mitigate electronic factors from the morphological study, the acceptor molecules **3a-e** are designed to be iso-energetic. Simple alkyl chains minimally impact electron density through resonance, and their influence through induction should be

similar, therefore very similar optoelectronic properties are expected. Such effects are confirmed by the characterization of their optical and electrochemical properties using UV-Vis spectroscopy and cyclic voltammetry. As shown in **Figure 1a**, the acceptors **3a**, **3b, 3d** and **3e** exhibit nearly identical absorption profiles, while a slight red-shift is observed in the spectrum of the benzyl substituted **3c**. This energetic shift may be ascribed to slight orbital overlap between the benzyl groups and the TBTA ring through homoconjugation.[37-38]

Cyclic voltammetric studies show that all the IDTT-TBTA acceptors have consistently reversible oxidation peaks, corresponding to a highest occupied molecular orbital (HOMO) energy level at approximately -5.5 eV, while irreversible reduction peaks indicate a LUMO level around -3.7 eV (**Figure 2a**). An energy level diagram compares the IDTT-TBTA acceptors to the donor polymer PCE10 (**Figure 2b**), showing the right alignment of the HOMO and LUMO levels of PCE10 with these of the acceptors (**Table 1**). A small energy offset between the LUMO levels of the donor and acceptors (<0.20 eV) is observed, though it has been shown that such a small offset can efficiently drive charge separation in non-fullerene acceptor based bulk heterojunctions.[39-42]

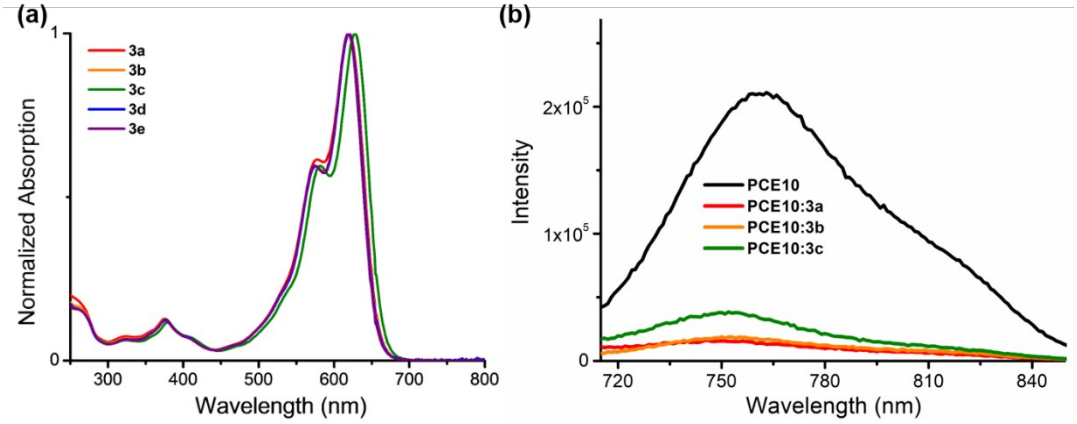

Figure 1. (a) Normalized UV-Vis spectra of NFA molecules **3a**-**e** (solvent: $CHCl_3$), and (b) photoluminescence spectra of pure PCE10 and mixtures of PCE10 with **3a**, **3b**, and **3c**.

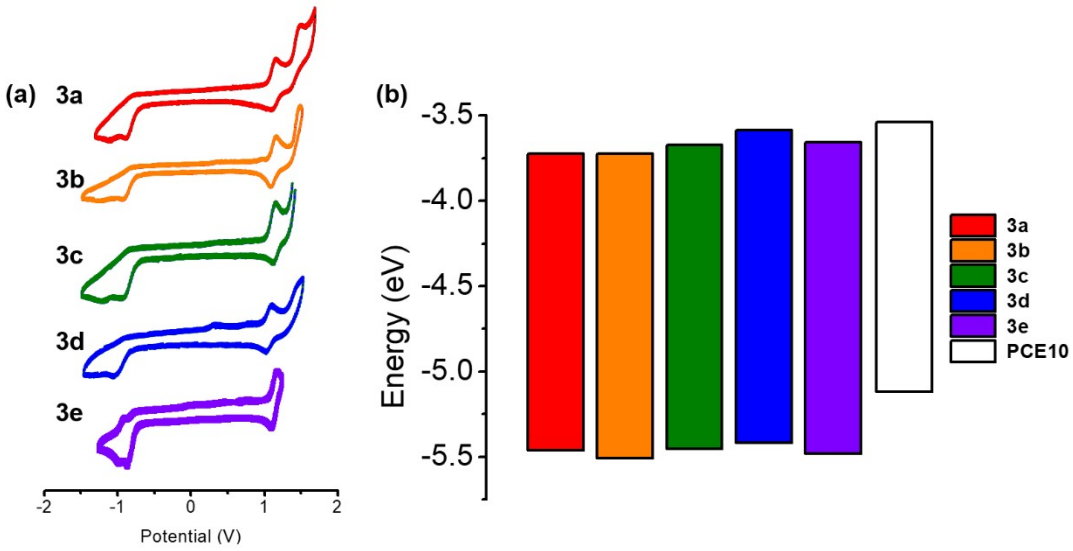

Figure 2. (a) Cyclic voltammetry of NFA **3a-e** (scan rate: 100 mV/s. Solvent: CH_2Cl_2). and (b) the energy alignment with PCE10 donor polymer.

Table 1. Frontier molecular orbital (FMO) energy levels for NFA and PCE10

Compound	Solubilizing group	HOMO (eV)	LUMO (eV)	E_g^{Elec} (eV)	E_g^{Opt} (eV)
3a	Methyl	-5.46	-3.72	1.74	1.89
3b	Ethyl	-5.51	-3.72	1.78	1.89
3c	Benzyl	-5.45	-3.67	1.78	1.87
3d	Octyl	-5.42	-3.59	1.83	1.89
3e	2-ethylhexyl	-5.48	-3.65	1.83	1.89
PCE10*	-	-5.23	-3.52	1.71	1.58

* from reference[43]

The effective charge transfer between the PCE10 donor and acceptors is confirmed by photoluminescence (PL) spectroscopy (**Figure 1b**). An obvious decrease in the intensity of the PCE10 fluorescence spectrum upon mixing with acceptors **3a**, **3b**, and **3c** shows that efficient charge transfer is occurring. Fluorescence quenching by methyl and ethyl derivatives are nearly equivalent and more efficient than the benzyl derivative.

Solar cell devices based on PCE10 and different acceptors are then fabricated with an inverted device structure of ITO/ZnO/PCE10:IDTT-TBTAs/MoOx/Ag. ITO is used as a transparent electrode with ZnO nanoparticles as the electron transport layer. Device performance is evaluated by plotting the current generated when the device is illuminated with respect to the voltage applied in the *J-V* curve (**Figure 3a**). The V_{OC}s of all acceptors are close or

above 1.00 V (**Table 2**), significantly larger than that of ITIC based devices, which has a V_{OC} of 0.825 V under these conditions. While V_{OC} is fairly consistent amongst acceptors, short circuit current (J_{SC}) and fill factor (FF) show large variations and are found to be highly dependent on the acceptor end group substitution. J_{SC} is a measure of the photocurrent and any factors that decrease mobility or carrier density, such as poorly defined domains, improper domain size, or high trap density, would depress J_{SC}. These factors are closely related to film morphology in nature. The highest J_{SC}s are associated with acceptors **3b** and **3c**, with significant drop for the acceptors with both shorter and longer alkyl chains. This Goldilocks zone implies that there is a balance of factors at play within the active layer. The fill factor precisely follows the same pattern as the J_{SC}. As the FF is a measure of resistive factors within the devices, any factors that worsen morphology will likewise lower the FF. Since all the solar cells have the same structure, resistive effects from the contacts can be discounted, making the FF a gauge of active layer resistances.

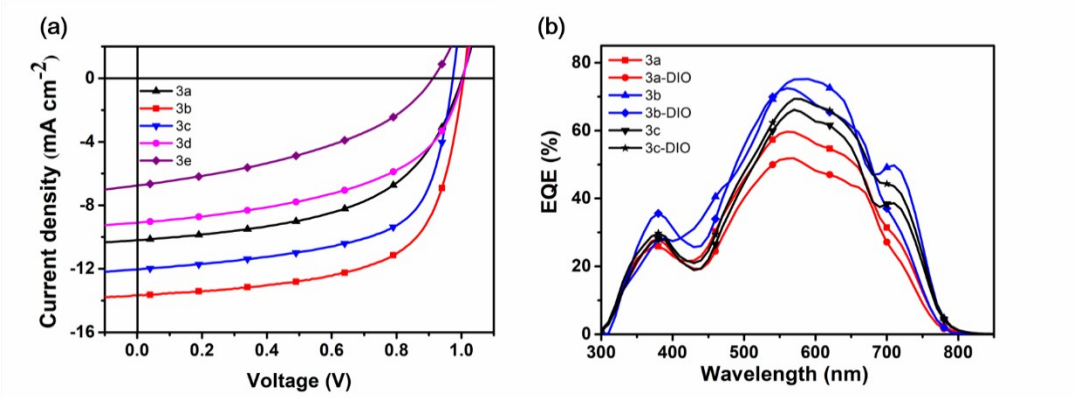

Figure 3. (a) *J-V* curve for optimized PCE10:NFA-based solar cells (1:1.5 ratio) under standard AM1.5 irradiation and (b) EQE curves for the devices based on NFAs **3a**, **3b**, and **3c** with or without DIO as the additive.

Table 2. Photovoltaic parameters of devices based on PCE10 and **3a-e** NFA.

Compound	Solubilizing group	DIO (wt %)	J_{SC} (mA cm^{-2})	V_{OC} (V)	FF (%)	PCE (%)
3a	Methyl	0	10.19	1.00	53.3	5.44 (5.31±0.15)
3b	Ethyl	0	13.70	1.00	64.0	8.77 (8.70±0.10)
3c	Benzyl	0	11.68	0.98	54.7	6.23 (6.13±0.12)
3c	Benzyl	0.5	12.04	0.97	63.2	7.41 (7.35±0.09)
3d	Octyl	0	9.10	1.01	51.3	4.69 (4.61±0.10)
3e	2-ethylhexyl	0	6.72	0.92	41.0	2.52 (2.38±0.16)

Considering the similar V_{OC}s between devices, the J_{SC} and FF are the most responsible metrics for the variations seen in efficiency.

The highest performing device uses **3b** as an acceptor and shows an efficiency of almost 9%. Both decreasing and increasing the alkyl chain length result in a lower efficiency, exclusively from decreases in the J_{SC} and FF. Since the active layer characteristics are primarily responsible for efficiency variations, a solvent additive, 1,8-diiodooctane (DIO) is employed in an attempt to improve film morphology. However, this additive has a negative impact on all active layers except the benzyl **3c** species, which presents a slight improvement with PCE enhanced from 6.23% to 7.41%. To understand the wavelength dependence on current generation, external quantum efficiency (EQE) has been determined for the three best performing acceptor-based devices (**Figure 3b**). The integrated current density in an EQE curve is in good agreement with the J_{SC} in a *J*-*V* plots (**Table S1**). The peak efficiency is between 500 and 700 nm, mainly corresponding to the acceptor absorption profile. This EQE feature confirms that the acceptor is a major contributor to current generation in this device.

To evaluate the charge carrier transporting behavior, hole-only and electron-only single carrier devices are fabricated for blends based on PCE10 and **3a**-**3b** with device structures of ITO/PEDOT:PSS/PCE10:IDTT-TBTAs/MoO_3/Al and ITO/ZnO/PCE10:IDTT-TBTAs/PFN-Br/Al, respectively. The mobility of films is measured in

the dark using the space charge limited current (SCLC) method. By fitting the current in the quadratic regime (**Figure S1**), the mobility can be calculated using the Mott-Gurney equation (**Equation 1**):[44]

$$J=\frac{9}{8}\mu\varepsilon_0\varepsilon_r\frac{V^2}{L^3} \quad (1)$$

where J is the current, ε_0 is the permittivity of free space, ε_r is the material relative permittivity, L is the thickness of the active layer, and V is the effective voltage. For the three PCE10:IDTT-TBTAs active layers, the mobilities of both electrons and holes are reasonably well matched, but with consistently higher hole mobilities (**Table S2**). The best electron and hole mobilities are observed for **3b**, which are also consistent with its highest solar cell performance. The electron and hole mobilities in the methyl alkylated **3a** are 7 and 5 times lower than then those observed for **3b**, supporting the hypothesis that inferior charge transport in the active layer is responsible for decreased J_{SC}, FF and PCE.

The high variability in metrics such as FF, J_{SC}, and charge mobility demands a closer study of film characteristics. Grazing incidence wide-angle X-ray scattering (GIWAXS) is a highly effective technique for probing the crystallinity of thin film samples with information on crystallite size, spacing between repeating units (*d*-spacing), and orientation with respect to the substrate. Both the

acceptor and polymer donor are observed to highly favor a face-on orientation. This is evident from a strong in-plane (100) lamellar stacking peak and the (010) out-of-plane π-π stacking peak (**Figure 4a**-**b** & **Figure 5a**-**b**). Face-on stacking is advantageous for solar cell performance since it allows for vertical charge transport within the device stack.[45-46] Same orientation adopted by both components is also favorable since mixing donor and acceptor components with different preferred orientation may result in lower efficiencies.[47-48]

To understand how the choice of alkyl chains affect film crystallinity, analysis of *d*-spacings and crystallite sizes is carried out. The (100) lamellar peak corresponds to horizontal edge-to-edge stacking (**Figure 4a**-**b**). By comparing the (100) *d*-spacing for the acceptors **3a**-**3e**, a pattern arises that is analogous to the relative trend in device efficiency and carrier mobility (**Figure 4c**). The acceptors **3b** and **3c** have the smallest *d*-spacing, and yield the highest performing devices. The *d*-spacing is higher for acceptors **3d** and **3e** with longer alkyl chains, as well as **3a** with a shorter methyl group, which correlates with lower device efficiency. The (100) diffraction feature of the acceptors in the mixed PCE10:acceptor systems is obscured by the (100) peak of the polymeric donor, nevertheless, the preservation of such diffraction feature provides certain insight about the effectiveness of donor-

acceptor mixing within the domains of the bulk heterojunction. Crystallite size analysis of the (100) peak of the pure acceptor thin films revels **3a** with a crystal correlation length (CCL) around three to four times larger than the other acceptors (**Figure 4d**). Unlike the other acceptors, when the acceptor **3a** is mixed with PCE10, the spectrum preserves almost all the spectrum features of the neat **3a** (**Figure 4e**). This lack of change in *d*-spacing and crystallite size for **3a** implies that there is minimal mixing between donor and acceptor domains which is a necessity for efficient charge separation.

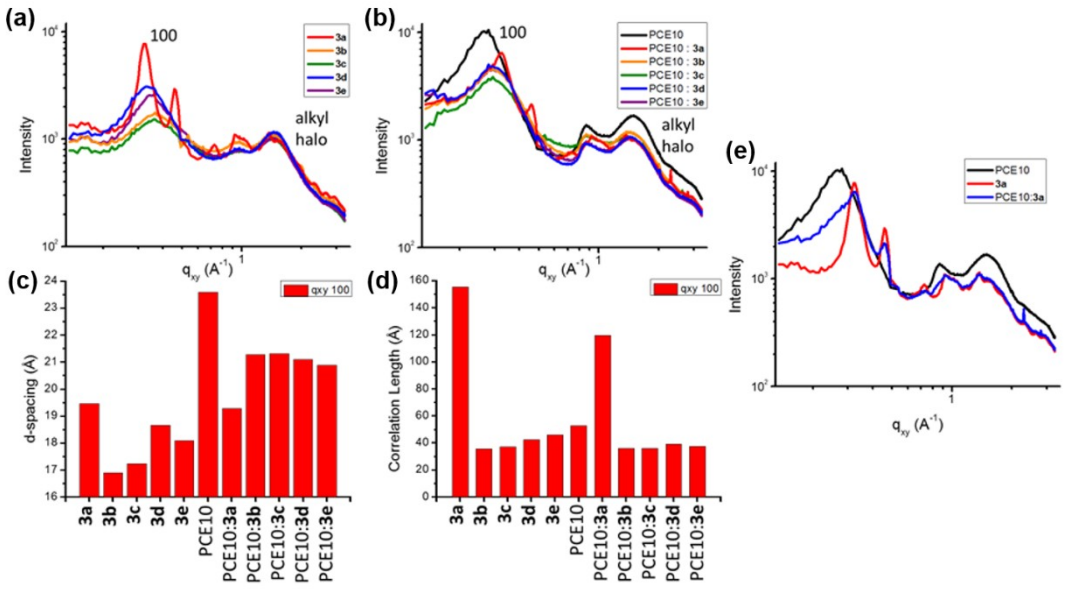

Figure 4. GIWAXS linecuts in the in-plane q_{xy} direction for (a) neat NFA **3a**-**3e**, and (b) mixtures of the acceptors with PCE10. Comparative analysis of (c) *d*-spacing and (d) crystal correlation length based on the (100) q_{xy} peak for pure acceptors, PCE10 donor, and the mixtures. (e) A superposition of q_{xy} linecuts of PCE10, **3a**

and the mixture.

The out-of-plane (010) diffraction peak corresponds to vertical π-π stacking (**Figure 5a**-**b**). While the acceptors **3b-3e** have wider π-π stacking *d*-spacings in the pure films, when mixed with the polymer donor, the corresponding *d*-spacings decrease, suggesting a tighter π-stacking due to domain mixing with the donor. The *d*-spacing decrease upon mixing is not observed for **3a**. Analysis of the crystal correlation length of the (010) peak can also illustrate some useful patterns (**Figure 5d**). The CCLs of acceptors alkylated with linear ethyl (**3b**) and *n*-octyl (**3d**) are nearly identical, which may be due to similar steric conditions close to the TBTA unit.[49] However, the branched 2-ethylhexyl acceptor **3e** has a smaller crystallite size, presumably due to the larger steric effect of branching alkyl chains. NFA **3c** also has a larger steric cone due to the benzyl group, potentially hindering π-π stacking in the solid state and decreasing the crystallite size. The pattern in crystallite size is consistent when mixed with PCE10, showing that the aggregation of the acceptors does have an effect on the overall mixture. The overlay of the diffraction patterns of the neat **3a** and the PCE10:**3a** blend (**Figure 5e**) shows that the *d*-spacings and crystallite sizes of **3a** remain constant, similar to the behavior of the (100) peak, further verifying

a lack of domain mixing for **3a**.

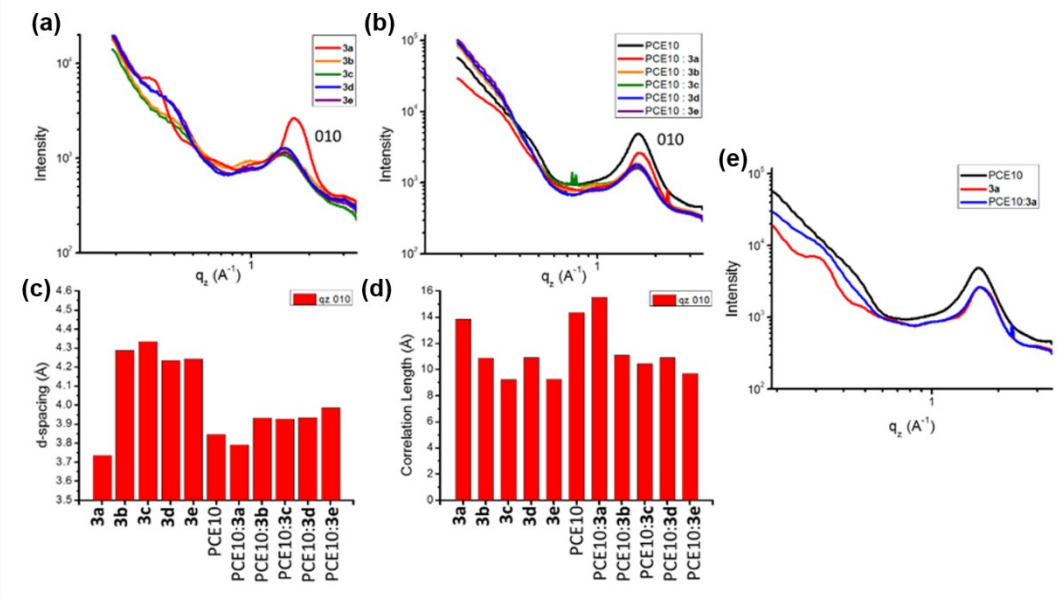

Figure 5. GIWAXS linecuts in the out-of-plane q_z direction for (a) neat NFA **3a**-**3e**, and (b) mixtures of the acceptors with PCE10. Comparative analysis of (c) *d*-spacing and (d) crystal correlation length based on the (010) q_z peak for pure acceptors, PCE10 donor, and mixtures. (e) A superposition of q_z linecuts of PCE10, **3a** and the mixture.

Atomic force microscopic (AFM) studies were carried out as a complementary characterization to analyze the film morphology. The AFM images of three pure films (3a, 3b and 3c) and three blend films, (PCE10:3a, PCE10:3b and PCE10:3c) were presented in Figure 6. The NFA 3a has the roughest surface with a root mean square (RMS) roughness of 4.7 nm, which corroborates with its large

crystallite size and the minimal mixing between PCE10 and 3a domains observed by GIWAXS studies. The NFA 3b and 3c form very smooth thin films as dictated by the substituents on the end groups. For the blend films of PCE10:3b and PCE10:3c, the RMS roughness increased slightly from 0.54 nm and 0.55 nm to 1.4 nm and 1.2 nm, respectively, both being smaller than that of the PCE10:3a blend (1.9 nm).

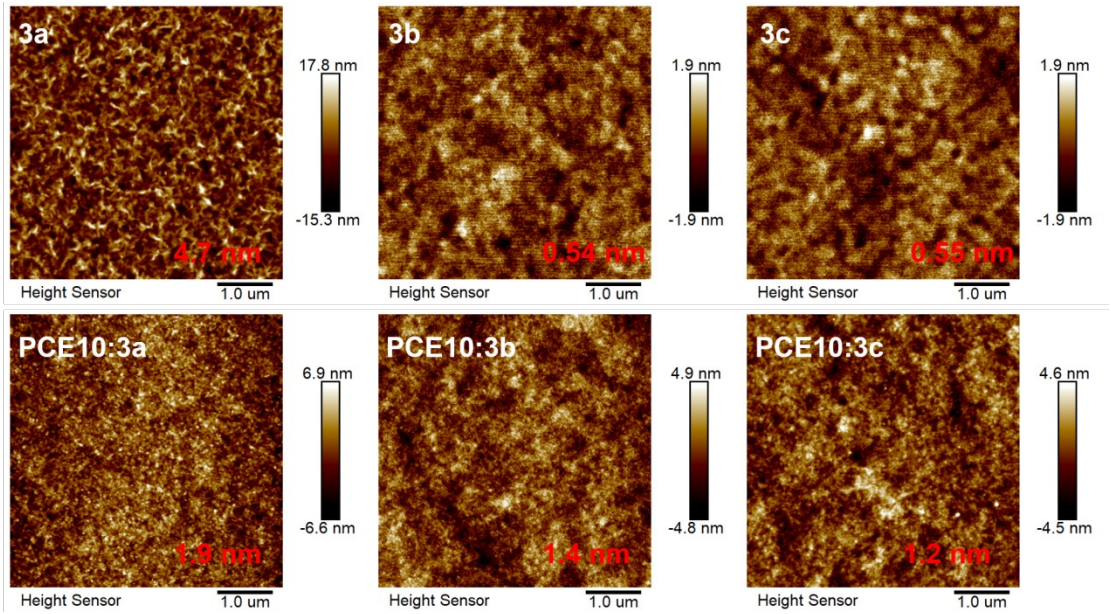

Figure 6. AFM height images of pure films of NFA 3a-3c and the corresponding blend films with PCE10.

From these results, a number of correlations arise that can help elucidate differences in device parameters. The trend in lamellar (100) peaks correlates well with the device performance, suggesting that the smaller intermolecular distances seen for **3b** and **3c** are

conducive for charge transfer in the devices. Additionally, the larger π-π stacking *d*-spacing distances seen for **3c** and **3e** are consistent with their inferior performance compared to their linear counterparts **3b** and **3d**, respectively. The methyl derivative **3a** is an outlier as significantly more crystalline than the others, with the shortest π-π stacking distance and the largest crystallite sizes in the series. Unlike the other acceptors, there is no evidence for mixing between donor and **3a** domains, which is a necessity for efficient charge separation (**Figures 4e, 5e**). The result of insufficient domain mixing and hard grain boundaries is likely the cause of the low performance of the PCE10:**3a** active layer.[50-52] This could also explain the poor mobilities, as completely isolated donor and acceptor domains are less likely to form a percolation pathway to allow for the flow of charges.

The photovoltaic performance and GIWAXS data paint a picture of how the alkyl chains of the end groups interact on a molecular level to determine properties on a materials level. The methyl substitution leads to highly crystalline materials, but so crystalline that there are insufficient mixed domains with the donor polymer. This mismatch results in low mobilities as well as depressed J_{SC}, FF, and PCE due to lower interfacial charge generation. At the other extreme, the octyl and 2-ethylhexyl substituted **3d** and **3e** are

observed to have wider lamellar stacking distances and π-π stacking distances when mixed with the donor polymer. This increased spacing between acceptor units and incorporation of additional insulating alkyl chains may be responsible for the low device performance. The acceptors **3b** and **3c** have crystallinity that straddles these two extremes, providing the optimal performance. The top performing acceptor **3b** has closer lamellar and π-π stacking than **3c**, correlating with the slightly improved charge transport and performance.

Conclusions

Introducing TBTA end groups to the IDTT core successfully increases the LUMO energy of these non-fullerene acceptors, greatly improving the V_{OC}. By interchanging the alkyl chains on the TBTA unit, a controlled morphological study is undertaken without altering the electronic properties. The corresponding device studies reveal that the ethyl and benzyl substituted acceptors **3b** and **3c** display superior performances compared to the other substituents, which correlate with small lamellar stacking distances and good heterojunction domain formation in the thin films.

Simply shortening the alkyl chains from ethyl to methyl groups in **3a** creates an acceptor that was too crystalline to form an ideal

heterojunction and significantly decreases the PCE. Conversely, acceptors **3d** and **3e** with longer alkyl chains show larger intermolecular distances, which lead to less efficient charge transfer. The TBTA with increased alkyl chain length from ethyl to *n*-octyl and 2-ethylhexyl results in a 46% and 71% decrease in efficiency, respectively. The insight provided in this study reveals the subtle substitution effect of the NFA end groups on thin film morphologies, which calls for a careful molecular approach when designing and screening materials for OSCs.

Experimental Section

Synthesis of 1c. Benzylamine (0.87 mL, 8.0 mmol, 2.0 equiv.) was added to an oven-dried flask equipped with a stirbar and a reflux condenser. After Toluene (10 mL) was added and the reaction mixture was cooled to 0 °C, carbon disulfide (0.24 mL, 4.0 mmol, 1.0 equiv.) was added and the reaction mixture was heated to 110 °C. After 12 hours the solution was cooled to ambient temperature and solid precipitated out of solution. The solution was concentrated to approximately 5 mL and filtered to yield a white crystalline solid (780 mg, 3.04 mmol, 76%). ^{1}H NMR (500 MHz, Chloroform-*d*) δ 7.37 – 7.21 (m, 10H), 6.01 (s, 2H), 4.63 (s, 4H). ^{13}C NMR (126 MHz, Chloroform-*d*) δ 182.01, 136.84, 129.09, 128.10, 127.68, 48.69.

HRMS for $C_{15}H_{16}N_2S$ (MALDI): $[M]^+$ Calcd: 256.1034, found 256.7882.

Synthesis of 1d. Octylamine (6.62 mL, 40.0 mmol, 2.0 equiv.) was added to an oven-dried flask equipped with a stirbar and a reflux condenser. Toluene (25 mL) and carbon disulfide (1.2 mL, 20 mmol, 1.0 equiv.) were added at room temperature and heated to 110 °C. After 12 hours the solution was cooled to ambient temperature and was concentrated to approximately 10 mL. The solid product was collected by filtration and washed with hexane to yield a white crystalline solid (4.85 g, 16.2 mmol, 81%). ^{1}H NMR (500 MHz, Chloroform-*d*) δ 6.05 (s, 1H), 3.36 (s, 2H), 1.55 (p, *J* = 7.4, 7.0 Hz, 2H), 1.30 – 1.19 (m, 11H), 0.83 (t, *J* = 6.9 Hz, 3H). ^{13}C NMR (126 MHz, Chloroform-*d*) δ 181.23, 44.57, 31.88, 29.36, 29.30, 29.14, 27.04, 22.74, 14.20. HRMS for $C_{17}H_{36}N_2S$ (MALDI): $[M]^+$ Calcd: 300.2599, found 300.9851.

Synthesis of 1e. 2-ethylhexylamine (1.31 mL, 8.00 mmol, 2.0 equiv.) was added to an oven-dried flask equipped with a stirbar and a reflux condenser. After toluene (5 mL) was added and cooled to 0 °C, carbon disulfide (0.24 mL, 4.0 mmol, 1.0 equiv.) was added and the reaction mixture was heated to 110 °C. After 12 hours the solution was cooled to ambient temperature and concentrated to yield a yellow oil that was used without further purification (1.21 g, 4.0 mmol, 100%). ^{1}H NMR (500 MHz, Chloroform-*d*) δ 5.72 (s, 2H),

3.33 (s, 4H), 1.58 – 1.52 (m, 2H), 1.42 – 1.32 (m, 4H), 1.35 – 1.22 (m, 12H), 0.89 (td, *J* = 7.0, 4.1 Hz, 12H). ^{13}C NMR (126 MHz, Chloroform-*d*) δ 181.86, 47.66, 39.25, 31.32, 29.08, 24.57, 23.21, 14.30, 11.12. HRMS for $C_{17}H_{36}N_2S$ (MALDI): $[M+H]^+$ Calcd: 301.2672, found 301.2464.

Synthesis of 2a. Dimethyl thiourea (1.0 g, 9.6 mmol, 1.0 equiv.) was added to a microwave vial, which was sealed with a septa cap and backfilled with nitrogen. A solution of sodium ethoxide in ethanol (21 wt%, 14.0 mL, 37.5 mmol, 3.9 equiv.) and diethyl malonate (5.86 mL, 38.4 mmol, 4 equiv.) were added sequentially and heated to reflux for 2 days. The crude reaction mixture was diluted with water and ethanol was removed via reduced pressure. The residue was acidified with HCl (1.0 M), extracted with ethyl acetate, dried over $MgSO_4$, and the solvent was removed under reduced pressure. The crude solid was recrystallized from chloroform to yield **2a** as white solid (1.21 g, 7.0 mmol, 73%), in an approximately 60:40 ratio of keto and enol forms. ^{1}H NMR (500 MHz, DMSO-d_6) δ 10.71 (s, 1H), 5.37 – 4.98 (m, 1H), 3.86 (s, 1H), 3.53 (s, 6H). ^{13}C NMR (126 MHz, DMSO-d_6) δ 182.41, 176.77, 164.80, 160.56, 82.20, 35.10. HRMS for $C_6H_8N_2O_2S$ (MALDI): $[M]^+$ Calcd: 172.0306, found 172.8449.

Synthesis of 2c. Benzyl thiourea (1.70 g, 6.65 mmol, 1.0 equiv.)

was added to a microwave vial, which was sealed with a septa cap and backfilled with nitrogen. A solution of sodium ethoxide in ethanol (21 wt%, 9.93 mL, 26.6 mmol, 4.0 equiv.) and diethyl malonate (4.05 mL, 26.6 mmol, 4.0 equiv.) were added sequentially and heated to reflux for 48 hours. The reaction was diluted with water and the ethanol was removed under reduced pressure. After the solid was removed by filtration, the filtrate was acidified with HCl (1.0 M), extracted with ethyl acetate, dried over $MgSO_4$ and the solvent was removed under reduced pressure. The crude reaction mixture was purified by column chromatography (0-100% ethyl acetate in hexanes) to yield a yellow viscous oil which crystallized over time (1.59 g, 4.89 mmol, 73%). ^{1}H NMR (500 MHz, Chloroform-*d*) δ 7.40 – 7.22 (m, 10H), 5.61 (s, 4H), 3.85 (s, 2H). ^{13}C NMR (126 MHz, Chloroform-*d*) δ 180.82, 163.60, 135.83, 128.54, 128.42, 127.86, 50.82, 40.72. HRMS for $C_{18}H_{16}N_2O_2S$ (MALDI): $[M+H]^+$ Calcd: 325.1005, found 325.1627.

Synthesis of 2d. Dioctyl thiourea (420 mg, 1.40 mmol, 1.0 equiv.) was added to a microwave vial, which was sealed with a septa cap and backfilled with nitrogen. Ethanol (2.0 mL), a solution of sodium ethoxide in ethanol (21 wt%, 2.24 mL, 6.0 mmol, 4.0 equiv.), and diethyl malonate (0.92 mL, 6.0 mmol, 4.0 equiv.) were added sequentially and heated to reflux for 4 days. The crude reaction

mixture was acidified with HCl (1.0 M), extracted with ethyl acetate, dried over $MgSO_4$ and the solvent was removed under reduced pressure. The crude reaction mixture was purified by column chromatography (0-100% ethyl acetate in hexane) to yield a yellow viscous oil which crystallized over time (160 mg, 0.43 mmol, 31%). ^{1}H NMR (500 MHz, Chloroform-*d*) δ 4.36 – 4.27 (m, 4H), 3.71 (s, 2H), 1.67 – 1.60 (m, 4H), 1.38 – 1.20 (m, 20H), 0.88 (t, *J* = 6.8 Hz, 6H). ^{13}C NMR (126 MHz, Chloroform-*d*) δ 180.62, 163.46, 48.37, 40.76, 32.02, 29.43, 29.38, 27.08, 27.00, 22.89, 14.37. HRMS for $C_{20}H_{36}N_2O_2S$ (MALDI): $[M+H]^+$ Calcd: 369.2570, found 369.2687.

Synthesis of 2e. 1,3-bis(2-ethylhexyl)thiourea thiourea (2.0 g, 6.6 mmol, 1.0 equiv.) was added to a microwave vial which was sealed with a septa cap and backfilled with nitrogen. Ethanol (6.7 mL), a solution of sodium ethoxide in ethanol (21 wt%, 9.93 mL, 26.6 mmol, 4.0 equiv.), and diethyl malonate (4.05 mL, 26.6 mmol, 4.0 equiv.) were added sequentially and heated to reflux for 48 hours. The reaction was diluted with water and ethanol was removed under reduced pressure. After the solid was removed by filtration, the filtrate was acidified with HCl (1.0 M), extracted with ethyl acetate, dried over $MgSO_4$ and the solvent was removed under reduced pressure. The crude reaction mixture was purified by column chromatography (0-20% ethyl acetate in hexanes) to yield a yellow

viscous oil (100 mg, 0.26 mmol, 4%). ^{1}H NMR (500 MHz, Chloroform-*d*) δ 4.37 – 4.24 (m, 4H), 3.74 (s, 2H), 1.97 (dt, *J* = 13.2, 6.6 Hz, 2H), 1.26 (pd, *J* = 21.3, 17.3, 9.8 Hz, 16H), 0.88 (h, *J* = 91 Hz, 12H). ^{13}C NMR (126 MHz, Chloroform-*d*) δ 181.61, 164.09, 51.36, 40.95, 37.06, 30.71, 28.76, 24.09, 23.32, 14.34, 10.89. HRMS for $C_{20}H_{36}N_2O_2S$ (MALDI): $[M+H]^+$ Calcd: 369.2570, found 369.2670.

Synthesis of 3a. ITIC dialdehyde (100 mg, 0.093 mmol, 1.0 equiv.) and ethyl TBTA (96 mg, 0.56 mmol, 6 equiv.) were added to an oven-dried round-bottom flask equipped with a reflux condenser and a stirbar. Chloroform (5 mL) was added, followed by the addition of pyridine (0.15 mL, 1.86 mmol, 20.0 equiv.). The resulting mixture was heated to 60 °C. After 24 hours the reaction was concentrated and purified by column chromatography (70-100% $CHCl_3$ in hexanes) to provide **3a** as blue solid (125 mg, 0.09 mmol, 97%). ^{1}H NMR (500 MHz, Chloroform-*d*) δ 8.69 (s, 2H), 8.14 (s, 2H), 7.64 (s, 2H), 7.22 (d, *J* = 8.3 Hz, 8H), 7.14 (d, *J* = 8.4 Hz, 8H), 3.81 (s, 8H), 3.80 (s, 8H), 2.60 – 2.53 (m, 8H), 1.59 (ddd, *J* = 13.0, 8.3, 6.3 Hz, 8H), 1.39 – 1.22 (m, 24H), 0.87 (t, *J* = 7.0, 6.1 Hz, 12H). ^{13}C NMR (126 MHz, Chloroform-*d*) δ 180.06, 161.76, 160.43, 155.86, 153.30, 150.37, 148.53, 147.75, 143.58, 142.69, 139.99, 139.11, 138.79, 137.05, 129.04, 128.07, 118.79, 109.68, 63.49, 36.28, 35.80, 35.53, 31.89, 31.46, 29.39, 22.79, 14.30. HRMS for $C_{82}H_{86}N_4O_4S_6$ (MALDI):

$[M]^+$ Calcd: 1383.5046, found 1383.7555.

Synthesis of 3b. ITIC dialdehyde (100 mg, 0.093 mmol, 1.0 equiv.) and ethyl TBTA (112 mg, 0.56 mmol, 6.0 equiv.) were added to an oven-dried round-bottom flask equipped with a reflux condenser and a stirbar. Chloroform (5.0 mL) was added, followed by the addition of pyridine (0.15 mL, 1.86 mmol, 20 equiv.). The reaction mixture was heated to 60 °C. After 24 hours the reaction was concentrated and purified by column chromatography (50-100% $CHCl_3$ in hexanes) to provide **3b** as blue solid (129 mg, 0.09 mmol, 96%). ^{1}H NMR (500 MHz, Chloroform-*d*) δ 8.67 (s, 2H), 8.16 (s, 2H), 7.67 (s, 2H), 7.26 (d, *J* = 8.3 Hz, 8H), 7.16 (d, *J* = 8.1 Hz, 8H), 4.60 (dq, *J* = 13.8, 6.9 Hz, 8H), 2.63 – 2.55 (m, 8H), 1.71 – 1.57 (m, 8H), 1.41 – 1.25 (m, 36H), 0.91 – 0.85 (m, 12H). ^{13}C NMR (126 MHz, Chloroform-*d*) δ 178.67, 161.15, 159.84, 155.74, 152.96, 149.83, 148.09, 147.67, 143.52, 142.64, 140.03, 139.16, 138.36, 136.99, 129.00, 128.07, 118.71, 110.24, 63.48, 44.16, 43.30, 35.78, 31.87, 31.44, 29.35, 22.77, 14.28, 12.69, 12.57. HRMS for $C_{86}H_{94}N_4O_4S_6$ (MALDI): $[M]^+$ Calcd: 1438.5599, found 1438.7133.

Synthesis of 3c. ITIC dialdehyde (100 mg, 0.093 mmol, 1.0 equiv.) and benzyl TBTA (181 mg, 0.56 mmol, 6.0 equiv.) were added to an oven-dried round-bottom flask equipped with a reflux condenser and a stirbar. Chloroform (5 mL) was added, followed by the addition of

pyridine (0.15 mL, 1.86 mmol, 20.0 equiv.). The resulting mixture was heated to 60 °C. After 24 hours the reaction was concentrated and purified by column chromatography (20-100% $CHCl_3$ in hexanes) to provide **3c** as blue solid (141 mg, 0.084 mmol, 90%). ^{1}H NMR (500 MHz, Chloroform-*d*) δ 8.73 (s, 2H), 8.13 (s, 2H), 7.72 (s, 2H), 7.48 – 7.39 (m, 8H), 7.38 – 7.27 (m, 20H), 7.18 (d, *J* = 8.1 Hz, 8H), 5.85 (s, 4H), 5.80 (s, 4H), 2.62 (t, *J* = 7.9 Hz, 8H), 1.64 (p, *J* = 7.9, 7.3 Hz, 8H), 1.42 – 1.32 (m, 24H), 0.95 – 0.90 (m, 12H). ^{13}C NMR (126 MHz, Chloroform-*d*) δ 179.44, 161.57, 160.23, 155.80, 153.34, 150.52, 148.50, 147.65, 143.66, 142.64, 140.06, 139.08, 138.69, 137.06, 136.63, 136.60, 128.99, 128.48, 128.46, 128.09, 128.02, 127.97, 127.47, 127.39, 118.79, 109.64, 63.43, 51.62, 50.60, 35.77, 31.86, 31.41, 29.37, 22.76, 14.29. HRMS for $C_{106}H_{102}N_4O_4S_6$ (MALDI): $[M]^+$ Calcd: 1686.6225, found 1686.9984.

Synthesis of 3d. ITIC dialdehyde (78 mg, 0.07 mmol, 1.0 equiv.) and octyl TBTA (160 mg, 0.43 mmol, 6.0 equiv.) were added to an oven-dried round-bottom flask equipped with a reflux condenser and a stirbar. Chloroform (4 mL) was added, followed by the addition of pyridine (0.11 mL, 1.4 mmol, 20 equiv.). The reaction mixture was heated to 60 °C. After 24 hours the reaction was concentrated and purified by column chromatography (0-100% $CHCl_3$ in hexanes) to provide **3d** as blue solid (125 mg, 0.07 mmol, 100%). ^{1}H NMR (500

MHz, Chloroform-*d*) δ 8.63 (s, 2H), 8.16 (s, 2H), 7.63 (s, 2H), 7.22 (d, *J* = 8.3 Hz, 8H), 7.13 (d, *J* = 8.3 Hz, 7H), 4.46 (dt, *J* = 10.7, 5.9 Hz, 8H), 2.60 – 2.53 (m, 8H), 1.75 – 1.69 (m, 10H), 1.62 – 1.56 (m, 4H), 1.45 – 1.22 (m, 64H), 0.92 – 0.82 (m, 24H). ^{13}C NMR (126 MHz, Chloroform-*d*) δ 179.09, 161.41, 159.96, 155.72, 152.86, 149.82, 148.11, 147.65, 143.55, 142.69, 140.10, 139.26, 138.16, 137.02, 129.03, 128.12, 118.73, 110.40, 63.51, 48.94, 48.07, 35.83, 32.09, 32.04, 31.91, 31.47, 29.53, 29.49, 29.45, 29.40, 27.19, 27.16, 27.10, 22.90, 22.88, 22.80, 14.36, 14.34, 14.30. HRMS for $C_{110}H_{142}N_4O_4S_6$ (MALDI): $[M+H]^+$ Calcd: 1775.9428, found 1775.1682.

Synthesis of 3e. ITIC dialdehyde (44 mg, 0.045 mmol, 1.0 equiv.) and benzyl TBTA (100 mg, 0.27 mmol, 6.0 equiv.) were added to an oven-dried round-bottom flask equipped with a reflux condenser and a stirbar. Chloroform (2.25 mL) was added, followed by the addition of pyridine (73 µL, 0.9 mmol, 20.0 equiv.) and the reaction mixture was heated to 60 °C. After 24 hours the reaction was concentrated and purified by column chromatography (20-100% $CHCl_3$ in hexanes) to provide **3e** as blue solid (63 mg, 0.035 mmol, 79%). ^{1}H NMR (500 MHz, Chloroform-*d*) δ 8.67 (s, 2H), 8.13 (s, 2H), 7.66 (s, 2H), 7.24 (dt, *J* = 8.9, 4.6 Hz, 9H), 7.14 (dd, *J* = 8.3, 3.3 Hz, 8H), 4.58 – 4.45 (m, 8H), 2.57 (td, *J* = 7.9, 1.9 Hz, 8H), 2.09 (ddd, *J* = 13.3, 6.5 Hz, 4H), 1.60 (dt, *J* = 33.4, 7.5, 6.9 Hz, 8H), 1.41 – 1.22 (m, 56H),

0.95 – 0.83 (m, 36H). ^{13}C NMR (126 MHz, Chloroform-*d*) δ 179.94, 179.92, 162.08, 160.60, 155.67, 152.73, 150.03, 148.08, 147.62, 143.43, 142.64, 142.62, 140.15, 139.28, 139.24, 138.13, 137.04, 128.99, 128.97, 128.12, 128.07, 118.70, 110.16, 63.44, 51.88, 50.83, 37.32, 37.29, 37.07, 35.81, 31.90, 31.46, 30.83, 30.67, 29.41, 29.38, 28.89, 28.79, 24.23, 24.03, 23.29, 22.79, 14.31, 11.02, 10.92. HRMS for $C_{110}H_{142}N_4O_4S_6$ (MALDI): $[M]^+$ Calcd: 1774.9355, found 1774.1312.

Solar cell fabrication. Solar cells were fabricated with an inverted device structure of ITO/ZnO/active layer/MoOx/Ag, where the ZnO electron transport layer was prepared through the sol-gel method and a molybdenum oxide hole transport layer was deposited via thermal evaporation. ITO coated glass substrates were cleaned prior to device fabrication by sonication in acetone, low concentration soap water, deionized water, and isopropyl alcohol and then dried in the oven. After treated in an ultraviolet-ozone chamber (Ultraviolet Ozone Cleaner, Jelight Company, USA) for 20 min, 40 nm of Sol-gel derived ZnO film was spin-casted on the ITO-coated glass substrates at 3000 rpm for 1 min. The substrates were subsequently dried at 200 °C for 1 hour in air and then transferred to a N_2-glovebox. The active layer was deposited via spin-coating. Finally, 10 nm molybdenum oxide (MoO_3) and 100 nm aluminum (Al) were

evaporated with a shadow mask as the top electrode. The active area was defined by the mask area of 0.16 cm^2.

Supporting Information

The Supporting Information is available free of charge on the ACS Publications website.

Additional experimental details, SCLC *J-V* curves, NMR spectra (PDF)

Conflicts of interest

There are no conflicts to declare.

Acknowledgements

This work was performed as a user project at the Molecular Foundry, Lawrence Berkeley National Laboratory, and GIWAXS data was collected at BL7.3.3 at Advanced Light Source, both being supported by the Office of Science, Office of Basic Energy Sciences, of the U. S. Department of Energy under Contract No. DE-AC02-05CH11231. L. X. thanks the financial support from the National Natural Science Foundation of China (51903057).

Reference

(1) Yu, G.; Gao, J.; Hummelen, J. C.; Wudl, F.; Heeger, A. J. Polymer Photovoltaic Cells: Enhanced Efficiencies via a Network of Internal Donor-Acceptor Heterojunctions. *Science* **1995,** *270*, 1789-1791.

(2) He, Z.; Xiao, B.; Liu, F.; Wu, H.; Yang, Y.; Xiao, S.; Wang, C.; Russell, T. P.; Cao, Y. Single-Junction Polymer Solar Cells with High Efficiency and Photovoltage. *Nat. Photonics* **2015,** *9*, 174-179.

(3) Liu, Y.; Zhao, J.; Li, Z.; Mu, C.; Ma, W.; Hu, H.; Jiang, K.; Lin, H.; Ade, H.; Yan, H. Aggregation and Morphology Control Enables Multiple Cases of High-Efficiency Polymer Solar Cells. *Nat. Commun.* **2014,** *5*, 5293-5300.

(4) Deng, D.; Zhang, Y.; Zhang, J.; Wang, Z.; Zhu, L.; Fang, J.; Xia, B.; Wang, Z.; Lu, K.; Ma, W. Fluorination-Enabled Optimal Morphology Leads to Over 11% Efficiency for Inverted Small-Molecule Organic Solar Cells. *Nat. Commun.* **2016,** *7*, 13740-13748.

(5) Xiao, L.; Lai, T.; Liu, X.; Liu, F.; Russell, T. P.; Liu, Y.; Huang, F.; Peng, X.; Cao, Y. A Low-Bandgap Dimeric Porphyrin Molecule for 10% Efficiency Solar Cells with Small Photon Energy Loss. *J. Mater. Chem. A.* **2018,** *6*, 18469-18478.

(6) He, Y.; Chen, H.-Y.; Hou, J.; Li, Y. Indene−C60 Bisadduct: a New Acceptor for High-Performance Polymer Solar Cells. *J. Am. Chem. Soc.* **2010,** *132*, 1377-1382.

(7) Liang, Y.; Xu, Z.; Xia, J.; Tsai, S. T.; Wu, Y.; Li, G.; Ray, C.; Yu, L. For the Bright Future—Bulk Heterojunction Polymer Solar Cells with Power Conversion Efficiency of 7.4%. *Adv. Mater.* **2010,** *22*, 135-138.

(8) Zhang, Q.; Kan, B.; Liu, F.; Long, G.; Wan, X.; Chen, X.; Zuo, Y.; Ni, W.; Zhang, H.; Li, M. Small-Molecule Solar Cells with Efficiency Over 9%. *Nat. Photonics* **2015,** *9*, 35-41.

(9) Zhao, J.; Li, Y.; Yang, G.; Jiang, K.; Lin, H.; Ade, H.; Ma, W.; Yan, H. Efficient Organic Solar Cells Processed from Hydrocarbon Solvents. *Nat. Energy* **2016,** *1*, 1-7.

(10) Chen, Z.; Cai, P.; Chen, J.; Liu, X.; Zhang, L.; Lan, L.; Peng, J.; Ma, Y.; Cao, Y. Low Band-Gap Conjugated Polymers with Strong Interchain Aggregation and Very High Hole Mobility Towards Highly Efficient Thick-Film Polymer Solar Cells. *Adv. Mater.* **2014,** *26*, 2586-2591.

(11) Xiao, L.; Chen, S.; Gao, K.; Peng, X.; Liu, F.; Cao, Y.; Wong, W.-Y.; Wong, W.-K.; Zhu, X. New Terthiophene-Conjugated Porphyrin Donors for Highly Efficient Organic Solar Cells. *Acs. Appl. Mater. Inter.* **2016,** *8*, 30176-30183.

(12) Sun, Y.; Welch, G. C.; Leong, W. L.; Takacs, C. J.; Bazan, G. C.; Heeger, A. J. Solution-Processed Small-Molecule Solar Cells with 6.7% Efficiency. *Nat. Mater.* **2012,** *11*, 44-48.

(13) Kyaw, A. K. K.; Wang, D. H.; Gupta, V.; Zhang, J.; Chand, S.; Bazan, G. C.; Heeger, A. J. Efficient Solution-Processed Small-Molecule Solar Cells with Inverted Structure. *Adv. Mater.* **2013,** *25*, 2397-2402.

(14) Wadsworth, A.; Moser, M.; Marks, A.; Little, M. S.; Gasparini, N.; Brabec, C. J.; Baran, D.; McCulloch, I. Critical Review of the Molecular Design Progress in Non-Fullerene Electron Acceptors Towards Commercially Viable Organic Solar Cells. *Chem. Soc. Rev.* **2019,** *48*, 1596-1625.

(15) Cheng, P.; Li, G.; Zhan, X.; Yang, Y. Next-Generation Organic Photovoltaics Based on Non-Fullerene Acceptors. *Nat. Photonics* **2018,** *12*, 131-142.

(16) Yuan, J.; Zhang, Y.; Zhou, L.; Zhang, G.; Yip, H.-L.; Lau, T.-K.; Lu, X.; Zhu, C.; Peng, H.; Johnson, P. A. Single-Junction Organic Solar Cell With Over 15% Efficiency Using Fused-Ring Acceptor with Electron-Deficient Core. *Joule* **2019,** *3*, 1140-1151.

(17) Jiang, K.; Wei, Q. Y.; Lai, J. Y. L.; Peng, Z. X.; Kim, H.; Yuan, J.; Ye, L.; Ade, H.; Zou, Y. P.; Yan, H. Alkyl Chain Tuning of Small Molecule Acceptors for Efficient Organic Solar Cells. *Joule* **2019,** *3*, 3020-3033.

(18) Cui, Y.; Yao, H.; Zhang, J.; Zhang, T.; Wang, Y.; Hong, L.; Xian, K.; Xu, B.; Zhang, S.; Peng, J. Over 16% Efficiency Organic Photovoltaic

Cells Enabled by a Chlorinated Acceptor with Increased Open-Circuit Voltages. *Nat. Commun.* **2019,** *10*, 2515-2522.

(19) Xu, X.; Feng, K.; Bi, Z.; Ma, W.; Zhang, G.; Peng, Q. Single-Junction Polymer Solar Cells with 16.35% Efficiency Enabled by a Platinum (Ii) Complexation Strategy. *Adv. Mater.* **2019,** *31*, 1901872-1901878.

(20) Hong, L.; Yao, H. F.; Wu, Z.; Cui, Y.; Zhang, T.; Xu, Y.; Yu, R. N.; Liao, Q.; Gao, B. W.; Xian, K. H.; Woo, H. Y.; Ge, Z. Y.; Hou, J. H. Eco-Compatible Solvent-Processed Organic Photovoltaic Cells with Over 16% Efficiency. *Adv. Mater.* **2019,** *31*. 1903441-1903447.

(21) An, Q.; Ma, X.; Gao, J.; Zhang, F. Solvent Additive-Free Ternary Polymer Solar Cells with 16.27% Efficiency. *Sci. Bull.* **2019,** *64*, 504-506.

(22) Chao, P.; Chen, H.; Zhu, Y.; Lai, H.; Mo, D.; Zheng, N.; Chang, X.; Meng, H.; He, F. A Benzo [1, 2-b: 4, 5-c′] Dithiophene-4, 8-Dione-Based Polymer Donor Achieving an Efficiency Over 16%. *Adv. Mater.* **2020**, 1907059-1907066.

(23) Liu, L.; Kan, Y.; Gao, K.; Wang, J.; Zhao, M.; Chen, H.; Zhao, C.; Jiu, T.; Jen, A. K. Y.; Li, Y. Graphdiyne Derivative as Multifunctional Solid Additive in Binary Organic Solar Cells with 17.3% Efficiency and High Reproductivity. *Adv. Mater.* **2020**, 1907604-1907610.

(24) Fan, B. B.; Zhang, D. F.; Li, M. J.; Zhong, W. K.; Zeng, Z. M. Y.;

Ying, L.; Huang, F.; Cao, Y. Achieving Over 16% Efficiency for Single-Junction Organic Solar Cells. *Sci. China Chem.* **2019,** *62*, 746-752.

(25) Ma, R.; Liu, T.; Luo, Z.; Guo, Q.; Xiao, Y.; Chen, Y.; Li, X.; Luo, S.; Lu, X.; Zhang, M. Improving Open-Circuit Voltage by a Chlorinated Polymer Donor Endows Binary Organic Solar Cells Efficiencies Over 17%. *Sci. China Chem.* **2020**, *62*, 325-330.

(26) Liu, Q. S.; Jiang, Y. F.; Jin, K.; Qin, J. Q.; Xu, J. G.; Li, W. T.; Xiong, J.; Liu, J. F.; Xiao, Z.; Sun, K.; Yang, S. F.; Zhang, X. T.; Ding, L. M. 18% Efficiency Organic Solar Cells. *Sci. Bull.* **2020,** *65*, 272-275.

(27) Lin, Y. Z.; Wang, J. Y.; Zhang, Z. G.; Bai, H. T.; Li, Y. F.; Zhu, D. B.; Zhan, X. W. An Electron Acceptor Challenging Fullerenes for Efficient Polymer Solar Cells. *Adv. Mater.* **2015,** *27*, 1170-1174.

(28) Tang, A.; Xiao, B.; Wang, Y.; Gao, F.; Tajima, K.; Bin, H.; Zhang, Z.-G.; Li, Y.; Wei, Z.; Zhou, E. Simultaneously Achieved High Open-Circuit Voltage and Efficient Charge Generation by Fine-Tuning Charge-Transfer Driving Force in Nonfullerene Polymer Solar Cells. *Adv. Funct. Mater.* **2018,** *28*, 1704507-1704515.

(29) Tang, A.; Song, W.; Xiao, B.; Guo, J.; Min, J.; Ge, Z.; Zhang, J.; Wei, Z.; Zhou, E. Benzotriazole-Based Acceptor and Donors, Coupled with Chlorination, Achieve a High VOC of 1.24 V and an Efficiency of 10.5% in Fullerene-Free Organic Solar Cells. *Chem Mater* **2019,** *31*, 3941-3947.

(30) Chen, Y.; Jiang, X.; Chen, X.; Zhou, J.; Tang, A.; Geng, Y.; Guo, Q.; Zhou, E. Modulation of Three p-Type Polymers Containing a Fluorinated-Thiophene-Fused-Benzotriazole Unit to Pair with a Benzotriazole-Based Non-fullerene Acceptor for High VOC Organic Solar Cells. *Macromolecules* **2019,** *52*, 8625-8630.

(31) Ni, W.; Li, M.; Kan, B.; Liu, F.; Wan, X.; Zhang, Q.; Zhang, H.; Russell, T. P.; Chen, Y. Fullerene-Free Small Molecule Organic Solar Cells with a High Open Circuit Voltage of 1.15 V. *Chem. Commun.* **2016,** *52*, 465-468.

(32) He, B.; Yang, B.; Kolaczkowski, M. A.; Anderson, C. A.; Klivansky, L. M.; Chen, T. L.; Brady, M. A.; Liu, Y. Molecular Engineering for Large Open-Circuit Voltage and Low Energy Loss in Around 10% Non-Fullerene Organic Photovoltaics. *Acs. Energy Lett.* **2018,** *3*, 1028-1035.

(33) Gong, Y.; Kan, Z.; Xu, W.; Wang, Y.; AlShammari, S. H.; Laquai, F.; Lai, W. Y.; Huang, W. Wide-Bandgap Small Molecular Acceptors Based on a Weak Electron-Withdrawing Moiety for Efficient Polymer Solar Cells. *Sol. RRL* **2018,** *2*, 1800120-1800127.

(34) Xiao, L.; He, B.; Hu, Q.; Maserati, L.; Zhao, Y.; Yang, B.; Kolaczkowski, M. A.; Anderson, C. L.; Borys, N. J.; Klivansky, L. M. Multiple Roles of a Non-Fullerene Acceptor Contribute Synergistically for High-Efficiency Ternary Organic Photovoltaics. *Joule* **2018,** *2*,

2154-2166.

(35) Yao, H.; Ye, L.; Hou, J.; Jang, B.; Han, G.; Cui, Y.; Su, G. M.; Wang, C.; Gao, B.; Yu, R. Achieving Highly Efficient Nonfullerene Organic Solar Cells with Improved Intermolecular Interaction and Open-Circuit Voltage. *Adv. Mater.* **2017,** *29*, 1700254-1700261.

(36) Klikar, M.; Jelinkova, V.; Ruzickova, Z.; Mikysek, T.; Pytela, O.; Ludwig, M.; Bures, F. Malonic Acid Derivatives on Duty as Electron-Withdrawing Units in Push-Pull Molecules. *Eur. J. Org. Chem.* **2017,** *2017*, 2764-2779.

(37) Yoon, M.-C.; Lee, S.; Tokuji, S.; Yorimitsu, H.; Osuka, A.; Kim, D. Homoconjugation in Diporphyrins: Excitonic Behaviors in Singly and Doubly Linked Zn(Ii)Porphyrin Dimers. *Chem. Sci.* **2013,** *4*, 1756-1764.

(38) Kawasumi, K.; Wu, T.; Zhu, T.; Chae, H. S.; Van Voorhis, T.; Baldo, M. A.; Swager, T. M. Thermally Activated Delayed Fluorescence Materials Based on Homoconjugation Effect of Donor–Acceptor Triptycenes. *J. Am. Chem. Soc.* **2015,** *137*, 11908-11911.

(39) Xiao, B.; Zhao, Y.; Tang, A.; Wang, H.; Yang, J.; Zhou, E. PTB7-Th Based Organic Solar Cell with a High Voc of 1.05 V by Modulating the LUMO Energy Level of Benzotriazole-Containing Non-Fullerene Acceptor. *Sci. Bull.* **2017,** *62*, 1275-1282.

(40) Gong, X.; Tong, M.; Brunetti, F. G.; Seo, J.; Sun, Y.; Moses, D.;

Wudl, F.; Heeger, A. J. Bulk Heterojunction Solar Cells with Large Open-Circuit Voltage: Electron Transfer with Small Donor-Acceptor Energy Offset. *Adv. Mater.* **2011,** *23*, 2272-2277.

(41) Menke, S. M.; Ran, N. A.; Bazan, G. C.; Friend, R. H. Understanding Energy Loss in Organic Solar Cells: Toward a New Efficiency Regime. *Joule* **2018,** *2*, 25-35.

(42) Xiao, L. G.; Mao, H. Y.; Li, Z. D.; Yan, C.; Liu, J.; Liu, Y. D.; Reimer, J. A.; Min, Y. G.; Liu, Y. Employing a Narrow-Band-Gap Mediator in Ternary Solar Cells for Enhanced Photovoltaic Performance. *Acs. Appl. Mater. Inter.* **2020,** *12*, 16387-16393.

(43) Hu, Z. H.; Wang, J.; Wang, Z.; Gao, W.; An, Q. S.; Zhang, M.; Ma, X. L.; Wang, J. X.; Miao, J. L.; Yang, C. L.; Zhang, F. J. Semitransparent Ternary Nonfullerene Polymer Solar Cells Exhibiting 9.40% Efficiency and 24.6% Average Visible Transmittance. *Nano Energy* **2019,** *55*, 424-432.

(44) Dacuña, J.; Salleo, A. Modeling Space-Charge-Limited Currents in Organic Semiconductors: Extracting Trap Density and Mobility. *Phys. Rev. B.* **2011,** *84*, 195209-195213.

(45) Tumbleston, J. R.; Collins, B. A.; Yang, L.; Stuart, A. C.; Gann, E.; Ma, W.; You, W.; Ade, H. The Influence of Molecular Orientation on Organic Bulk Heterojunction Solar Cells. *Nat. Photonics* **2014,** *8*, 385-391.

(46) Vohra, V.; Kawashima, K.; Kakara, T.; Koganezawa, T.; Osaka, I.; Takimiya, K.; Murata, H. Efficient Inverted Polymer Solar Cells Employing Favourable Molecular Orientation. *Nat. Photonics* **2015,** *9*, 403-408.

(47) Yang, Y. M.; Chen, W.; Dou, L.; Chang, W.-H.; Duan, H.-S.; Bob, B.; Li, G.; Yang, Y. High-Performance Multiple-Donor Bulk Heterojunction Solar Cells. *Nat. Photonics* **2015,** *9*, 190-198.

(48) Salleo, A. Charge Transport in Polymeric Transistors. *Mater. Today* **2007,** *10*, 38-45.

(49) Harper, K. C.; Bess, E. N.; Sigman, M. S. Multidimensional Steric Parameters in The Analysis of Asymmetric Catalytic Reactions. *Nat. Chem.* **2012,** *4*, 366-374.

(50) Bourque, A. J.; Engmann, S.; Fuster, A.; Snyder, C. R.; Richter, L. J.; Geraghty, P. B.; Jones, D. J. Morphology of a Thermally Stable Small Molecule OPV Blend Comprising a Liquid Crystalline Donor and Fullerene Acceptor. *J. Mater. Chem. A.* **2019,** *7*, 16458-16471.

(51) Moulé, A. J.; Meerholz, K. Controlling Morphology in Polymer–Fullerene Mixtures. *Adv. Mater.* **2008,** *20*, 240-245.

(52) Xiao, L.; Li, Z.; Hu, Q.; Liu, Y.; Zhong, W.; Mei, X.; Russell, T. P.; Liu, Y.; Min, Y.; Peng, X. Improving the Efficiencies of Small Molecule Solar Cells by Solvent Vapor Annealing to Enhance J-Aggregation. *J. Mater. Chem. C.* **2019,** *7*, 9618-9624.

For Table of Contents Only